SCHRÖDINGER EQUATION FOR THE CHIRAL GEOMETRY IN ATOMIC NUCLEI

Radu BUDACA[1]

Abstract. The dynamical and spectral features of the chiral geometry in atomic nuclei are described by means of a triaxial rigid rotor Hamiltonian cranked by quasiparticle alignments. The problem is treated alternatively in the space of angular momentum states and using a Schrödinger equation for a continuous variable associated with an angular momentum projection. The later is constructed using a semiclassical approach. Numerical applications performed for various deformation and alignment conditions with both methods are compared in terms of energy levels and wave functions.

Keywords: Chiral geometry, Triaxiality, Semiclassical description

DOI 10.56082/annalsarsciphyschem.2024.1.7

1. Introduction

The concept of chirality or handedness is related to the asymmetry properties of a system. Basically, a chiral system is distinct from its mirror image. This property is systematically encountered in nature and subsequently is important in most domains of science. One of the most immediate examples of chirality are the human hands. Shells of snails, spirals and coils of plant veins, or flower formations are other macroscopic biological ensembles with a chiral geometry. From mathematical point of view, a system is chiral if its mirror image cannot be obtained by a combination of only translation and rotation transformations. In science, the chirality is more often invoked in molecular and biological chemistry, where chiral partners of compound molecules often exhibit drastically different properties such as smell, taste, or colour. A notable example of a chiral biological molecule, is the DNA double helix. The chirality in physics is mostly associated with spin dynamics and the polarization of the electromagnetic waves.

In nuclear physics, chirality is related to the trihedral geometry of three mutually perpendicular angular momentum vectors corresponding to the core rotation and two distinct spins coming from out of core nucleons. The three vectors can therefore be arranged into a right-handed or left-handed order. Given the fact that vectors are involved instead of coordinate loci, the nuclear chirality is of the dynamical type. The two chiral configurations in this case can be obtained from each other through a rotation and a time reversal transformation instead of a space inversion employed for

[1] rbudaca@theory.nipne.ro, budacaradu@gmail.com "Horia Hulubei" National Institute for R&D in Physics and Nuclear Engineering, Str. Reactorului 30, RO-077125, POB-MG6 Bucharest-Măgurele, Romania; Academy of Romanian Scientists, Splaiul Independentei 54, 050044, Bucharest, Romania

the static chirality. The conditions in which the three spin vectors achieve a mutual orthogonality were originally proposed by Frauendorf and Meng [1]. It all comes down to the quasiparticle nature of the nucleons which couple to the triaxial core. More precisely, a nucleon of particle (hole) nature will rotate around the short (long) axis of the mean field generated by the triaxial core, which in turn favors the rotation around its medium body-fixed axis with the maximal moment of inertia (MOI). The schematic representation of such a geometrical arrangement is given in Fig. 1.

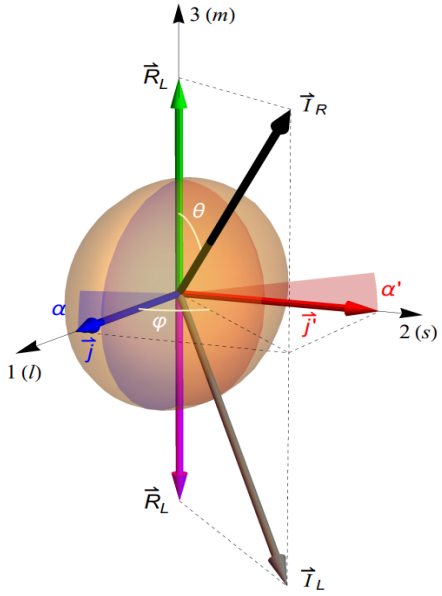

Figure 1: Schematic representation of the chiral geometry in atomic nuclei. Right- (R) and left-handed (L) configurations of rotor ($\vec{R}$) and total ($\vec{I}$) angular momentum vectors are correspondingly labeled. For the direction of the total angular momentum vector one also pointed out the stereographic variables φ and θ. The considered departure from the perfect orthogonal alignment of the single particle spins ($\vec{j}$) and ($\vec{j}'$) is also presented.

The two chiral configurations can be related either by the interchange between the quasiparticle alignments or considering an opposite rotation for the triaxial core. The distinction between the two opposite chirality configurations is valid in the body fixed frame of reference, but are indistinguishable in the laboratory reference system where the measurements are taken. Due to the restoration of the chiral symmetry, a degenerated pair of $\Delta I = 1$ rotational bands of the same parity should be observed. The first observation of such bands and consequently the experimental realization of chiral geometry was reported in a few $N = 75$ odd-odd nuclei [2]. This event triggered a concerted theoretical and experimental effort for establishing the extent of this dynamical mode in other nuclei. As a result, chiral bands are presently identified in more than fifty nuclei [3, 4], be it in its originally proposed one proton

and one neutron configuration, or with multiple quasiparticle alignments. Most of the experimental realizations can be localized within the so called islands of chirality centered on the mass numbers A = 80, 100, 130 and 190 with specific single-particle states involved in the realization of the chiral geometry. The quasiparticle alignments are usually generated by protons and neutrons from intruder orbitals $g_{9/2}$, $h_{11/2}$, and $i_{13/2}$, assuring thus a high spin contribution to the total angular momentum of the system. The topic of nuclear chirality evolved also to a point where it is considered in connection to other nuclear structure properties or phenomena such as octupole correlations [5], shape phase transitions [6] and shape coexistence phenomena [7], or softness of the triaxial deformation [8].

The expected degeneracy of the chiral bands is rarely experimentally realized, being confirmed only approximately for few nuclei in limited ranges of total angular momentum. Nevertheless, the chiral assignment of these bands persisted due to the same underlying structure. At low spins, the core rotation is slow and the two chiral configurations are attained as turning points for the so called chiral vibration [2]. The excited state of the same angular momentum and parity is shifted in this case with a vibrational energy. With the increase of core's rotation, the chiral directions of the total angular momentum stabilize, marking thus the beginning of the static chirality regime. The lack of degeneracy between the partner bands in this high spin regime can be ascribed to the deviations from perfect orthogonality of the all three vectors involved in the chiral geometry. Indeed, the uniform rotation of the core is plagued by precession components coming from its triaxiality [9, 10, 11, 12, 13], while the fractional occupancies of the coupled quasiparticles induce tilting to their assumed axial alignments [14]. Of course, in this situation the system is no longer chiral, but valuable information can be extracted having this picture in mind.

Although the obvious theoretical tool to approach the chiral geometry in atomic nuclei is the Particle-Rotor Model (PRM) [15], its interpretation regarding the direction of the total angular momentum in relation with the nuclear density distribution was achieved using the Tilted Axis Approach (TAC) [16]. On one hand, the quantum nature of the PRM offers spectral signatures and selection rules for the electromagnetic properties of the chiral partner bands [17, 18, 19, 20, 21, 22]. On the other hand, the semiclassical upbringing of the TAC formalism is able to unveil the dynamical behaviour of the chiral system [23, 24, 25, 26]. Advances in understanding and describing the properties of chiral bands were driven by various approximations and extensions of these two models such as TAC plus random phase approximation [27, 28], collective Hamiltonian [29, 30, 31], boson expansion [32, 33], projected mean-field [34, 35, 36], and semiclassical models [9, 10, 37, 38]. Alternative theoretical approaches to those based on PRM and TAC such as the Interacting Boson Model [39, 40, 41] must also be mentioned.

The semiclassical approaches deserve a special attention due to their ability to combine the advantages of the PRM and TAC formalisms. This is achieved by

ascribing to the original quantum PRM Hamiltonian a classical picture in terms of directional angles of the total angular momentum vector, from which the dynamics of the system can be better understood. The semiclassical method can also be used to recast the original quantum PRM Hamiltonian into a Schrödinger equation for a suitably chosen continuous variable, which can calculate experimental observables and relate them with the underlying classical motion. The same program had great success in the description of the wobbling excitations [42, 43, 44, 45, 46], a phenomenon having many common features with the nuclear chirality. To keep the formalism tractable, a frozen approximation is usually adopted for the quasiparticle spins, which actually relates the PRM and TAC approaches. Indeed, with adoption of rigid or frozen quasiparticle alignments, the PRM Hamiltonian becomes a cranked rotor Hamiltonian with constraints defined by the quasiparticle alignments. Such a model is then well suited for the investigation of realistic arrangements of the implicated spin vectors deviating from the perfect chiral geometry. The analytical formalism behind this quantum model is presented in Section 2. The construction of the Schrödinger equation associated to this quantum problem, by means of a semiclassical procedure, is detailed in Section 3. Given the fact that in order to obtain a Schrödinger equation, one must adopt additional approximation and perform a requantization, it is interesting to compare the eigensystems of the two approaches. This is the main focus of the study and is realized in Section 4 with various numerical applications. The conclusions of this comparison are synthesized in the last section.

2. Constrained triaxial rotor model for chiral geometry

The interaction between the rotation of a triaxial core and two quasiparticle ($\vec{j}$) and ($\vec{j'}$), is usually described by an appropriate extension of the PRM:

$$H = H_R + H_{qp} + H'_{qp} \tag{2.1}$$

The first term

$$H_R = \sum_{k=1,2,3} A_k (\hat{I}_k - \hat{j}_k - \hat{j'}_k)^2 \tag{2.2}$$

is the triaxial rotor Hamiltonian for the core angular momentum ($\vec{R}$)= ($\vec{I}$) - ($\vec{j'}$) - ($\vec{j'}$) , with ($\vec{I}$) being the total spin of the system. Each principal axis rotation component is factorized by the corresponding inertial parameter $A_k = 1/(2\mathcal{J}_k)$, which is related to the moment of inertia

$$\mathcal{J}_k = \frac{4}{3}\mathcal{J}_0 \sin^2\left(\gamma - \frac{2}{3}k\pi\right), \tag{2.3}$$

defined in the hydrodynamic model [15] with the help of the triaxiality measure γ. The shapes of the triaxial core repeat themselves at $\gamma = \pi/3$ intervals, with redistributed axis assignments. The correspondence between the MOI and the core's shape can be tracked with the help of the semi-axis lengths:

$$R_k = R_0 \left[1 + \sqrt{\frac{5}{4\pi}} \beta \cos\left(\gamma - \frac{2\pi}{3} k \right) \right], \tag{2.4}$$

where β is the axial deformation. This allows the identification of the intrinsic axes as the long (l), short (s) and medium (m) depending on the value of the triaxiality measure γ. A triaxial rigid body will favor rotations around the medium intrinsic principal axis whose MOI is maximal. For the purpose of the present study, the third axis is chosen as a quantization axis and associated with the rotation of the core. The third axis become medium for $\gamma \in (60^\circ,\ 120^\circ)$, implying $R_2 < R_3 < R_1$, such that the other two axes 1 and 2, become long and respectively short. The alignment of the single-particle spins is determined by their quasiparticle character [47] as follows: a hole quasiparticle will rotate around the l axis, a particle around the s axis, while a nucleon in the vicinity of the Fermi surface will prefer rotations around the m axis.

In what follows, the quasiparticle spins are considered rigidly aligned in respect to the body-fixed system of reference. This condition, also referred to as the frozen alignment (FA) approximation, is realized by replacing the quasiparticle spin operators with their expectation values associated with the assumed alignment geometry. The perfect chiral geometry emerges when one quasiparticle is fully aligned to the s axis and another one to the l axis, with the core favoring rotations around the m axis. To encompass a more realistic situation, the spins of the quasiparticles are considered rigidly aligned along the principal planes 1-3 and 2-3 as in Fig. 1, with α and α_0 angles accounting for the deviations from the full l and s axial alignments:

$$\begin{aligned} \hat{j}_1 &= j_1 \cos\alpha,\ \hat{j'}_1 = 0, \\ \hat{j}_2 &= 0,\ \hat{j'}_2 = j' \cos\alpha', \\ \hat{j}_3 &= j \sin\alpha,\ \hat{j'}_3 = j' \sin\alpha'. \end{aligned} \tag{2.5}$$

The FA assumption reduces the relevant part of the PRM Hamiltonian to [37]:

$$\begin{aligned} \hat{H}_{align} &= A_1 \hat{I}_1^2 + A_2 \hat{I}_2^2 + A_3 \hat{I}_3^2 - 2A_1 j \hat{I}_1 \cos\alpha - 2A_2 j' \hat{I}_2 \cos\alpha' \\ &\quad -2A_3 (j \sin\alpha + j' \sin\alpha') \hat{I}_3, \end{aligned} \tag{2.6}$$

where one omitted the constant quasiparticle contribution. This operator defines a cranked rotor Hamiltonian for a total spin $\hat{I}$, whose constraining terms originate from the quasiparticle alignments. In this way, the single-particle degrees of freedom are downgraded to perturbing effects for the total angular momentum. The Hamiltonian $\hat{H}_{align}$ can be diagonalized for each angular momentum value I, in a basis of $2I+1$ rotation states $|IMK\rangle$, where M and K are projections in the laboratory

and respectively body-fixed reference frame of the $\hat{I}_3$. The matrix elements of the $\widehat{H}_{align}$ can be expressed as:

$$\begin{aligned}
&\langle IMK|\ddot{H}_{align}|IMK'\rangle = \\
&\left[\frac{A_1+A_2}{2}\left(I^2+I-K^2\right)+A_3K\left(K-2j\sin\alpha-2j'\sin\alpha'\right)\right]\delta_{K,K'} \\
&+\frac{A_1-A_2}{4}\left[\sqrt{(I+K+2)(I-K-1)(I+K+1)(I-K)}\delta_{K,K'-2}\right. \\
&\left.+\sqrt{(I-K+2)(I+K-1)(I-K+1)(I+K)}\delta_{K,K'+2}\right] \\
&-A_1j\cos\alpha\left[\sqrt{(I+K+1)(I-K)}\delta_{K,K'-1}+\sqrt{(I-K-1)(I+K)}\delta_{K,K'+1}\right] \\
&-iA_2j'\cos\alpha'\left[\sqrt{(I+K+1)(I-K)}\delta_{K,K'-1}-\sqrt{(I-K-1)(I+K)}\delta_{K,K'+1}\right].
\end{aligned} \tag{2.7}$$

The corresponding wave function is

$$|\Phi_{IMs}\rangle = \sum_{K=-I}^{I}\Lambda_{IKs}|IKM\rangle, \tag{2.8}$$

where s is the solution's order and Λ_{IKs} are the corresponding eigenvector components.

3. Schrödinger equation for a projection variable

In order to obtain an alternative quantum description of the dynamics associated with the $\widehat{H}_{align}$ Hamiltonian, one must pass through a semiclassical description. This stage introduces a new restricted set of complex variables, which will be ultimately quantized. The semiclassical description is based on a time-dependent variational principle [48]

$$\delta\int_0^t\left\langle\psi\left|\hat{H}_{align}-\frac{\partial}{\partial t'}\right|\psi\right\rangle dt'=0, \tag{3.1}$$

applied to the $\widehat{H}_{align}$ Hamiltonian with an appropriately chosen variational state. The coherent state for the angular momentum operators is the standard choice for the variational state [9, 10]:

$$\begin{aligned}
|\psi_{IM}(x,\varphi)\rangle &= \left(\frac{I+x}{2I}\right)^I e^{\sqrt{\frac{I+x}{I-x}}e^{i\varphi}\hat{I}_-}|IMI\rangle \\
&= \sum_{K=-I}^{I}\frac{1}{(2I)^I}\sqrt{\frac{(2I)!}{(I-K)!(I+K)!}}(I+x)^{\frac{I-K}{2}}(I-x)^{\frac{I+K}{2}}e^{i\varphi(I+K)}|IMK\rangle.
\end{aligned} \tag{3.2}$$

Here one used the stereographic parametrization of the complex coordinates in terms of the azimuth angle φ and a polar projection variable $x = I\cos\theta$ of the total angular momentum vector on the third (quantization) axis. Solving the variational principle, one obtains a classical counterpart of the quantum Hamiltonian $\widehat{H}_{align}$,

represented by an energy function depending on the stereographic variables of the variational function:

$$\begin{aligned}\mathcal{H}(x,\varphi) &= \langle\Psi_{IM}(x,\varphi)|H_{align}|\Psi_{IM}(x,\varphi)\rangle \\ &= \frac{(2I-1)(I^2-x^2)}{2I}(A_1\cos^2\varphi + A_2\sin^2\varphi - A_3) \\ &\quad -2\sqrt{I^2-x^2}(A_1 j\cos\alpha\cos\varphi + A_2 j'\cos\alpha'\sin\varphi) \\ &\quad -2A_3 x(j\sin\alpha + j'\sin\alpha') + \frac{I}{2}(A_1+A_2) + A_3 I^2,\end{aligned} \tag{3.3}$$

where $\hbar = 1$ is assumed. The other product of the variational principle is a pair of equations of motion,

$$\{\mathcal{H}, x\} = \dot{x}, \;\; \{\mathcal{H}, \varphi\} = \dot{\varphi}, \tag{3.4}$$

which are expressed with the help of the Poisson bracket. Note the canonical form of the equations of motion, which is due to the chosen variables. Consequently, these variables are canonically conjugated $\{\varphi, x\} = 1$, and one can assign x as being the generalized momentum, while φ as the generalized coordinate. This property is further used to quantize the classical energy function by means of a correspondence principle between the canonical variables and their differential operator counterparts. The procedure is however not straightforward, because the classical energy function have products of mixed rational and trigonometric functions of momentum and coordinate. In order to pass this obstacle, one recounts the properties of the classical energy function. It can be thus shown that the classical energy function (3.3) always has a single minimum in φ when γ is restricted to the $(60^\circ,120^\circ)$ interval. The classical energy function can be then approximated by means of a harmonic expansion around the corresponding minimum points in $\varphi_0(x)$ for fixed values of x:

$$\tilde{\mathcal{H}}(x,\varphi) \approx \mathcal{H}(x,\varphi_0(x)) + \frac{1}{2}\left(\frac{\partial^2\mathcal{H}}{\partial\varphi^2}\right)_{\varphi_0(x)}[\varphi-\varphi_0(x)]^2 . \tag{3.5}$$

With this, the trigonometric functions are replaced by powers of φ, up to the second order. The minimum path function $\varphi_0(x)$ is defined as the solution of a quartic equation for $\cos\varphi_0(x)$:

$$\begin{aligned}&(2I-1)\sqrt{I^2-x^2}(A_2-A_1)\cos\varphi_0(x)\sin\varphi_0(x) \\ &= 2I\left[A_2 j'\cos\varphi_0(x)\cos\alpha' - A_1 j\sin\varphi_0(x)\cos\alpha\right],\end{aligned} \tag{3.6}$$

which originates from the minimum condition $\partial H(x,\varphi)/\partial\varphi = 0$. The role of the

harmonic approximation is twofold. Indeed, the classical energy approximated as a second order function in φ, can now be quantized into a Schrödinger equation in the momentum space. Symmetrizing the mixed products of coordinate and momentum, and then applying the correspondence principle $\varphi = i\frac{d}{dx}$, one arrives at the following differential equation:

$$-\frac{1}{2B(x)}\frac{d^2F(x)}{dx^2}+\left(\frac{B'(x)}{2\left[B(x)\right]^2}-\frac{i\varphi_0(x)}{B(x)}\right)\frac{dF(x)}{dx}+\left[\mathcal{H}(x,\varphi_0(x))+\frac{\left[\varphi_0(x)\right]^2-i\varphi_0(x)}{2B(x)}+\frac{i\varphi_0(x)B'(x)}{2\left[B(x)\right]^2}+\frac{B''(x)}{4\left[B(x)\right]^2}-\frac{\left[B'(x)\right]^2}{2\left[B(x)\right]^3}\right]F(x)=EF(x), \tag{3.7}$$

For an unknown wave function $F(x)$. Prime and double prime denote x derivatives. Making the change of function

$$f(x)=\left[B(x)\right]^{-\frac{1}{4}}F(x)e^{i\int\varphi_0(x)dx}, \tag{3.8}$$

one can see that

$$\begin{aligned} B(x) &= \left[\frac{\partial^2\mathcal{H}(x,\varphi)}{\partial\varphi^2}\right]^{-1}_{\varphi_0(x)} \\ &= \left\{\frac{2I-1}{I}(I^2-x^2)(A_2-A_1)\cos 2\varphi_0(x)+2\sqrt{I^2-x^2}\right. \\ &\quad \left.\times\left[A_1 j\cos\varphi_0(x)\cos\alpha+A_2 j'\sin\varphi_0(x)\cos\alpha'\right]\right\}^{-1}, \end{aligned} \tag{3.9}$$

plays the role of a coordinate dependent effective mass for the Schrödinger equation:

$$\left[-\frac{1}{2}\frac{1}{\sqrt{B(x)}}\frac{d}{dx}\frac{1}{\sqrt{B(x)}}\frac{d}{dx}+V(x)\right]f(x)=Ef(x). \tag{3.10}$$

The effective mass defines the potential

$$V(x)=\mathcal{H}(x,\varphi_0(x))+\frac{B''(x)}{8\left[B(x)\right]^2}-\frac{9\left[B'(x)\right]^2}{32\left[B(x)\right]^3}, \tag{3.11}$$

and is also involved in the normalization condition for the new wave-function

$$\int_{-I}^{I} |f(x)|^2 \sqrt{B(x)} dx = 1. \tag{3.12}$$

The Hamiltonian of Eq.(3.10) is similar to those constructed based on TAC formalism [29, 30, 31], but is completely determined just by the deformation and the alignment geometry of the treated system.

If $\varphi_0(x)$ is known, then the two quantities $B(x)$ and $V(x)$ can be analytically described. When $\gamma = 90^\circ$ ($A_1 = A_2 = A_{1,2}$), Eq.(3.6) has a simple solution, represented by a constant $\tan \Phi_0 = \frac{j' cos\alpha'}{j cos\alpha}$. Moreover, the potential $V(x)$ acquires in this case a relatively simple compact expression:

$$V(x) = v_0 + v_1 x + v_2 \sqrt{I^2 - x^2} + v_3 x^2 + v_4 \frac{1}{\sqrt{I^2 - x^2}} + v_5 \frac{x^2}{(I^2 - x^2)^{3/2}}, \tag{3.13}$$

where

$$\begin{aligned} v_0 &= A_{1,2} I^2 + \frac{I}{2}(A_3 - A_{1,2}), & v_3 &= \frac{2I-1}{2I}(A_3 - A_{1,2}), \\ v_1 &= -2A_3 \left(j \sin\alpha + j' \sin\alpha'\right), & v_4 &= -\frac{v_2}{8}, \\ v_2 &= -2A_{1,2}\sqrt{j^2 \cos^2\alpha + j'^2 \cos^2\alpha'}, & v_5 &= \frac{17 v_2}{32}. \end{aligned} \tag{3.14}$$

The corresponding mass function is also simplified:

$$B(x) = \frac{1}{\sqrt{2(I^2 - x^2)} A_{1,2} (j \cos\alpha + j' \cos\alpha')}. \tag{3.15}$$

Note that B(x) is invariant to the change $x \rightleftarrows -x$, while $V(x)$ is not. This aspect is actually generally valid, regardless of the triaxial deformation γ.

However, for a $\gamma \neq 90°$, Eq.(3.6) must be solved numerically. Only one out of its four solutions is real and physically relevant. A continuous and differentiable instance of $\varphi_0(x)$ to be used in the above definitions of the effective mass and potential is obtained as follows. The selected solution is calculated for each angular momentum in an extended array of values for x. As can be seen from the Eq.(3.6), the minimum condition is symmetric to the change $\pm x$, therefore one can limit the calculation only to $x \in [0, I)$. These points are then interpolated with a spline function. Few instances of the $\varphi_0(x)$ are shown in Fig.2. It is clear that the effect of the tilting becomes important only at high angles, being materialized in an extension of the functions's range.

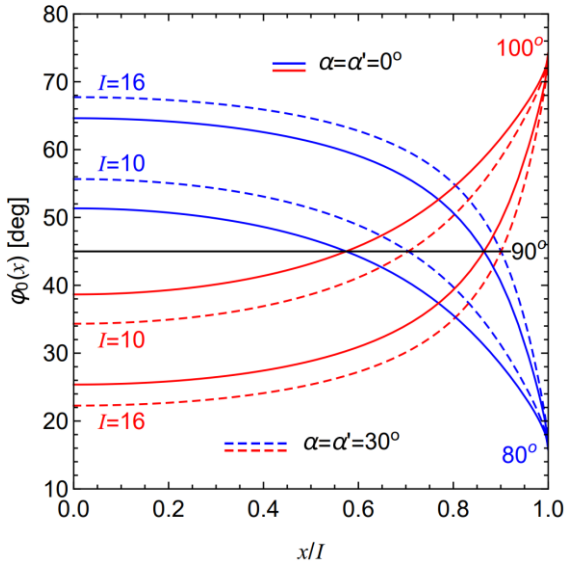

Figure 2: Solution $\varphi_0(x)$ of Eq.(3.6) for $j = j' = 11/2$ and selected values of the triaxiality parameter $\gamma = 80°, 90°, 100°$, angular momentum $I = 10$ and 16, with and without tilting.

The natural boundary $|x| \leq I$ of the problem [49] leads to the inevitable choice of particle in the box wave-functions:

$$f_I^s(x) = F_I^s(x)\,[B(x)]^{-\frac{1}{4}} = \frac{[B(x)]^{-\frac{1}{4}}}{\sqrt{I}} \left\{ \sum_{n=1}^{n_{Max}} A_n^s \cos\left[\frac{(2n-1)\pi x}{2I}\right] + \sum_{n=1}^{n_{Max}} B_n^s \sin\left[\frac{2n\pi x}{2I}\right] \right\}, \tag{3.16}$$

or the diagonalization basis. These functions satisfy the Dirichlet boundary condition $F_I^s\,(I) = F_I^s(-I) = 0$.

The basis dimension is truncated when a satisfactory convergence of eigenvalues is achieved. Previous numerical applications of the model established that a hundred basis states assures a satisfactory convergence of the diagonalization results for all relevant deformation and alignment conditions. The order s of the diagonalization solutions distinguishes the energy states belonging to distinct chiral bands. For a meaningful comparison with the exact diagonalization results, one expresses the total wave function as an expansion in rotation states

$$|\Psi_{IMs}\rangle = \sum_{K=-I}^{I} \Lambda_{IKs} |IKM\rangle. \tag{3.17}$$

The expansion coefficients

$$\Lambda_{IKs} = \left[\sum_{K=-I}^{I} \rho_I^s(K) \right]^{-\frac{1}{2}} F_I^s(K), \tag{3.18}$$

are determined with the help of the continuous probability distribution

$$\rho_I^s(x) = |F_I^s(x)|^2 = |f_I^s(x)|^2 \sqrt{B(x)}, \tag{3.19}$$

resulting from the diagonalization of the Schrödinger equation.

4. Numerical application

The energy splitting between the yrast and yrare partner bands

$$\Delta E(I) = E_{s=2}(I) - E_{s=1}(I), \tag{4.1}$$

is calculated by means of the two methods presented above for different alignment geometry and triaxiality. For this task one chosen the most common quasiparticle configuration of one proton and one neutron with $j = j' = 11/$. The results of the exact diagonalization procedure and that obtained with the Schrödinger equation are visualized in Fig.3. First of all, one must remark the strong effect of even a small amount of tilting. Indeed, the degeneracy of the partner states achieved at high spins when the quasiparticle alignments are axial, is transformed into an increasing energy shift as a function of total angular momentum, regardless of the method.
The exact calculations are overestimated in the chiral vibration region represented by the decrease of the energy difference with spin, and then underestimated in the higher spin regime, where few distinct dynamical scenarios can occur depending on the tilting. As the most experimental data are encompassed in the first vibrational regime, a suitable adjustment of the scale $1/\mathcal{J}_0$ can in principle achieve an approximate equivalence between the two approaches. Comparing the whole spectrum, one observes that the minimum in the energy difference which marks the end of the chiral vibration regime is shifted to higher angular momentum values in comparison to the exact diagonalization results. The discrepancy between two calculations at higher spins increases for larger tilting angles. Nevertheless, the Schrödinger equation results exhibit the same qualitative behavior as a function of total angular momentum as the exact problem.

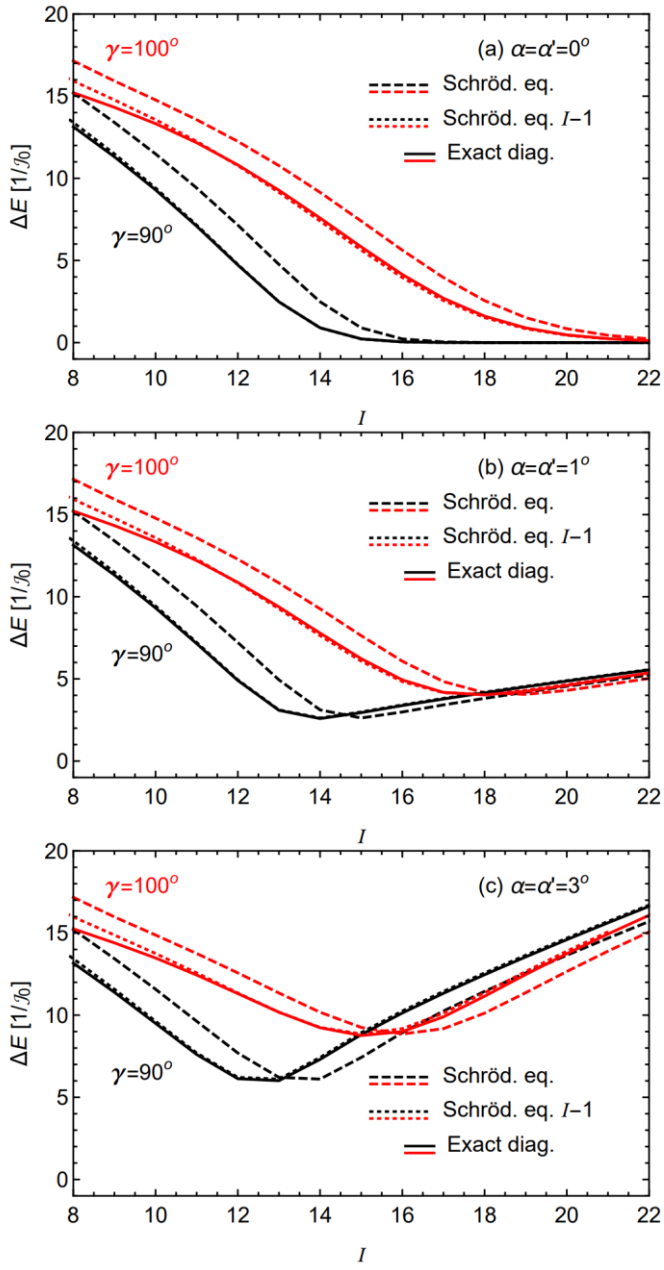

Figure 3: The energy splitting of the chiral bands with $j = j' = 11/2$ as a function of angular momentum, determined within the Schrödinger equation and the exact diagonalization for $\gamma = 90°$, 100° and tilting angles $\alpha = \alpha' = 0°$ (a), 1° (b), 3° (c). The Schrödinger equation results shifted to I — 1 position are also given as a reference.

A close inspection of Fig.3 suggests that the two calculations are congruent within a positive translation of angular momentum $\delta I \approx 1$ in the case of the Schrödinger problem. More precisely, the results of the exact diagonalization for an angular momentum I is equivalent with the results for the Schrödinger equation corresponding to $I + 1$. This relationship can be traced back to the dequantization and quantization procedures leading to the Schrödinger picture, where the uncertainty principle changes the original meaning of the angular momentum [46]. The correspondence $I \rightleftarrows I + 1$ between the two results is indeed one to one for the most part of the angular momentum range. Only the initial low spin part slightly deviates from this rule for more axially symmetric deformation ($\gamma \gtrless 90°$). As the diagonalization of the Schrödinger equation is significantly more computationally demanding than the exact diagonalization of the original cranked rotor Hamiltonian, their relationship can be used to determine model parameters of the first more easily. The usefulness of the more intricate Schrödinger picture resides in the separation of the kinetic and potential energy for a continuous variable associated with the total angular momentum projection, which allows the phenomenological interpretation of the quantum states in terms of anharmonic oscillations of the total angular momentum vector [38, 46]. The absolute energies visualized in Fig.4, are quite different in the two approaches. The excitation energies in the ground and excited bands obtained within the Schrödinger equation approach agree with those of the exact diagonalization mostly for very triaxial deformations $\gamma = 90° \pm 5°$ and low angular momentum states. The ground band levels calculated in the space of angular momentum states are underestimated up to $I = 13$ and $I = 12$ for axial and $\alpha = \alpha' = 3°$ quasiparticle alignments when maximal triaxiality $\gamma = 90°$ is assumed. Above these levels the exact excitation energies begin to be increasingly underestimated. This relationship depends on the triaxial deformation, such that at sufficiently axial deformation ($\gamma > 90°$) all exact diagonalization excitation energies become underestimated. This is the result of the contradictory evolution of the energy spectrum from maximal triaxiality to more axial deformation. Indeed, Fig.4 (a) and (c) shows that the Schrödinger equation spectrum becomes more compressed with the increase of γ, while the exact diagonalization spectrum become slightly expanded at low spins. In comparison to the ground band, the exact diagonalization results for the levels of the excited band are all underestimated. Excited energy levels of the exact diagonalization increase with the γ deformation, whereas those coming from the Schrödinger equation have a similar behaviour only for axial alignments. When tilting is present, the excited states from the Schrödinger equation behave quit erratically at more axial deformations. As can be observed in Fig.4 (d), the Schrödinger equation spectrum for large values of γ, is elevated in energy at low spins and lowered in energy at higher spins. A more general comparison between the axial and non axial alignment results, reveals the fact that the Schrödinger equation approximates better the

ground band for axial alignments and the excited band for tilted alignments.

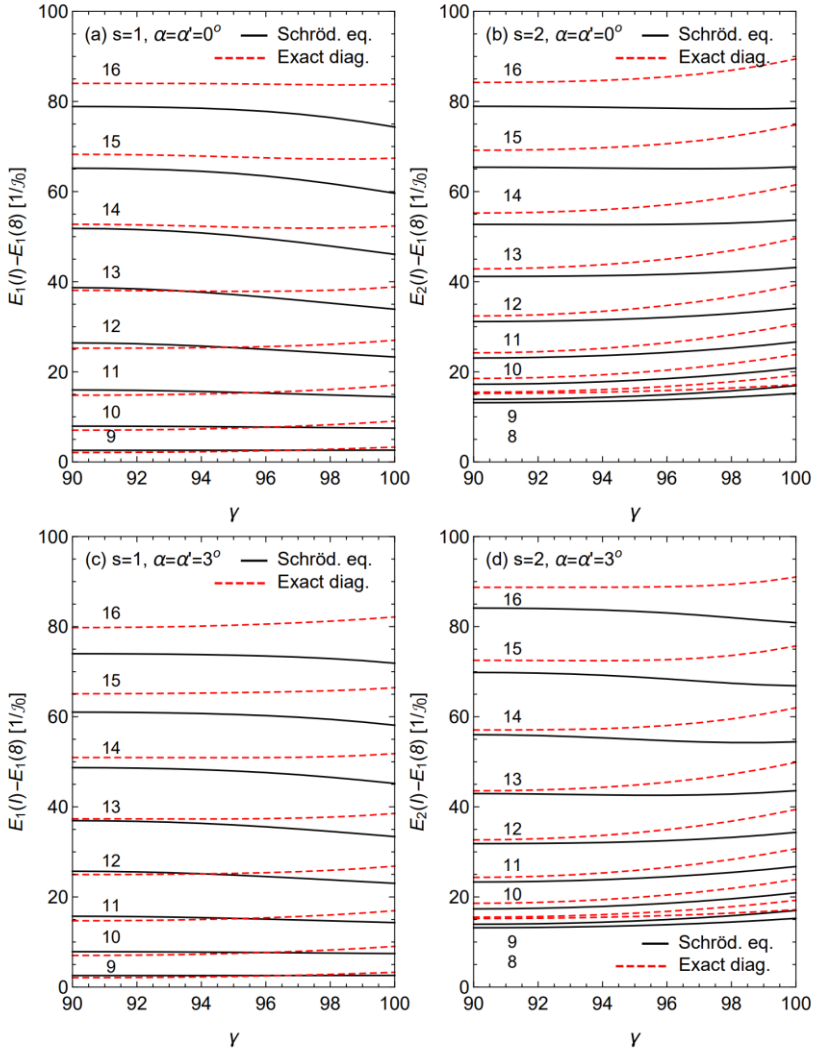

Figure 4: Energy spectra of the ground band for axial (a) and tilted (c) alignments, and of the excited band for axial (b) and tilted (d) alignments, as a function of deformation γ. The absolute energies are calculated for $j = j' = 11/2$ and given in units of $1/\mathcal{J}_0$ in reference to the ground band level $I = 8$.

In order to demonstrate the practical usefulness of the Schrödinger equation approach, one considers here a particular numerical application performed on the observed partner bands in the ^{138}Pm nucleus [50]. Previous descriptions of the chiral bands in this nucleus performed with the Schrödinger equation approach [37, 38], considered maximal triaxiality $\gamma = 90°$ and established that one of the quasiparticles

is axially aligned, while the other has a sizable ≈ 8° tilting. Note that due to the fact that at $\gamma = 90°$, two MOI are equal ($A_1 = A_2$), the problem with $j = j'$ cannot distinguish which quasiparticle is tilted, as the two alignment possibilities become equivalent. A microscopic investigation of the two chiral partner bands must be invoked in order to make an informed choice for the tilted quasiparticle. The findings of Ref.[51] can perfectly serve this role, which established that the dominant quasiparticle configuration in the structure of the chiral partner bands in ^{138}Pm is represented by a proton particle $h_{11/2}$ spin with a substantial deviation from the *s* axis. Therefore the tilting in the present model for this nucleus is associated with the quasiparticle spin j'. The energy difference between the two partner bands obtained form fitting experimental data for ^{138}Pm, is confronted with the corresponding experimental quantity in Fig.5. The model reproduces correctly the evolution with spin of ΔE, including the decreasing part associated with the chiral vibration, the increasing part corresponding to the stabilized rotations, and the correct position of the minimum marking the transition between the two distinct regimes. Fig.5 also shows the energy difference resulting from the exact diagonalization of the original Hamiltonian containing angular momentum operators with the same scaling, alignment and deformation parameters. As was previously pointed out, these results shifts the minimum to lower angular momentum but qualitatively presents the same behaviour. It is worth to emphasize the fact that the evolution of the observed energy difference cannot be reproduced with considering tilting.

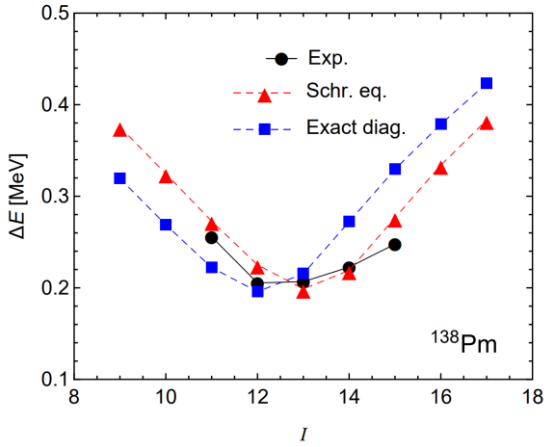

Figure 5: The evolution of the experimental energy difference between partner bands of the ^{138}Pm nucleus [50] as a function of total angular momentum is compared with the results of Schrödinger equation fits as well as with associated exact diagonalizetion results. The theoretical results correspond to $\mathcal{J}_0 = 35.68$ MeV^{-1} and tilting angles $\alpha = 0°$, $\alpha' = 8°$.

Beside the energy levels, it is also instructive to compare the wave-functions resulting from the two formalisms. This is done in Fig.6, where one compared the coefficients of the total wave function expansion in rotation matrices obtained from exact diagonalization of the cranked rotor Hamiltonian and those resulted from the continuous density probability distribution offered by the Schrödinger equation. The results are shown only for the states with experimental chiral partners. It is remarkable to find that the two approaches are very much alike, with a predilection for higher K values in case of the exact diagonalization expansion coefficients. The ground band states have a single peak initially localized around $K = 0$ and which moves to positive K values with the increasing of total spin. On the other hand, the chiral partner states exhibit a node separating two peaks. This structure is well known to be associated with vibrational excitations, where the two peaks correspond to the turning points of the classical oscillation. The interpretation of this regime as vibrational cannot be confidently deduced from the discrete distribution of the K components, but it is naturally emerging from the continuous density distribution coming from the Schrödinger equation. This is one of the advantages of the Schrödinger equation over the solution of the problem in discrete angular momentum states. However, as spin increases, one of the two peaks starts to disappear by feeding the other. The surviving peak is opposite to the one from the ground band. One can therefore affirm that there is a transition from a chiral vibration to a static rotation where the two partner states achieve opposite handedness.

The phenomenological analysis of the states resulting from the Schrödinger equation is completed by plotting in Fig.7, the chiral potential and the effective mass associated with angular momentum states considered in Fig.6. The transition between vibrational regime and the stable rotation mode discussed above can now be better understood by correlating it with the evolution of the chiral potential. The potential have a single asymmetric minimum at the lowest spin state and then starts to develop a second $x < 0$ minimum higher in energy. At higher spins, the second well completely traps the excited state forcing a stable rotation with $K < 0$ on it. In what concerns the symmetric mass function, it evolves from a flat shape towards a more parabolic x dependence as angular momentum is decreased.

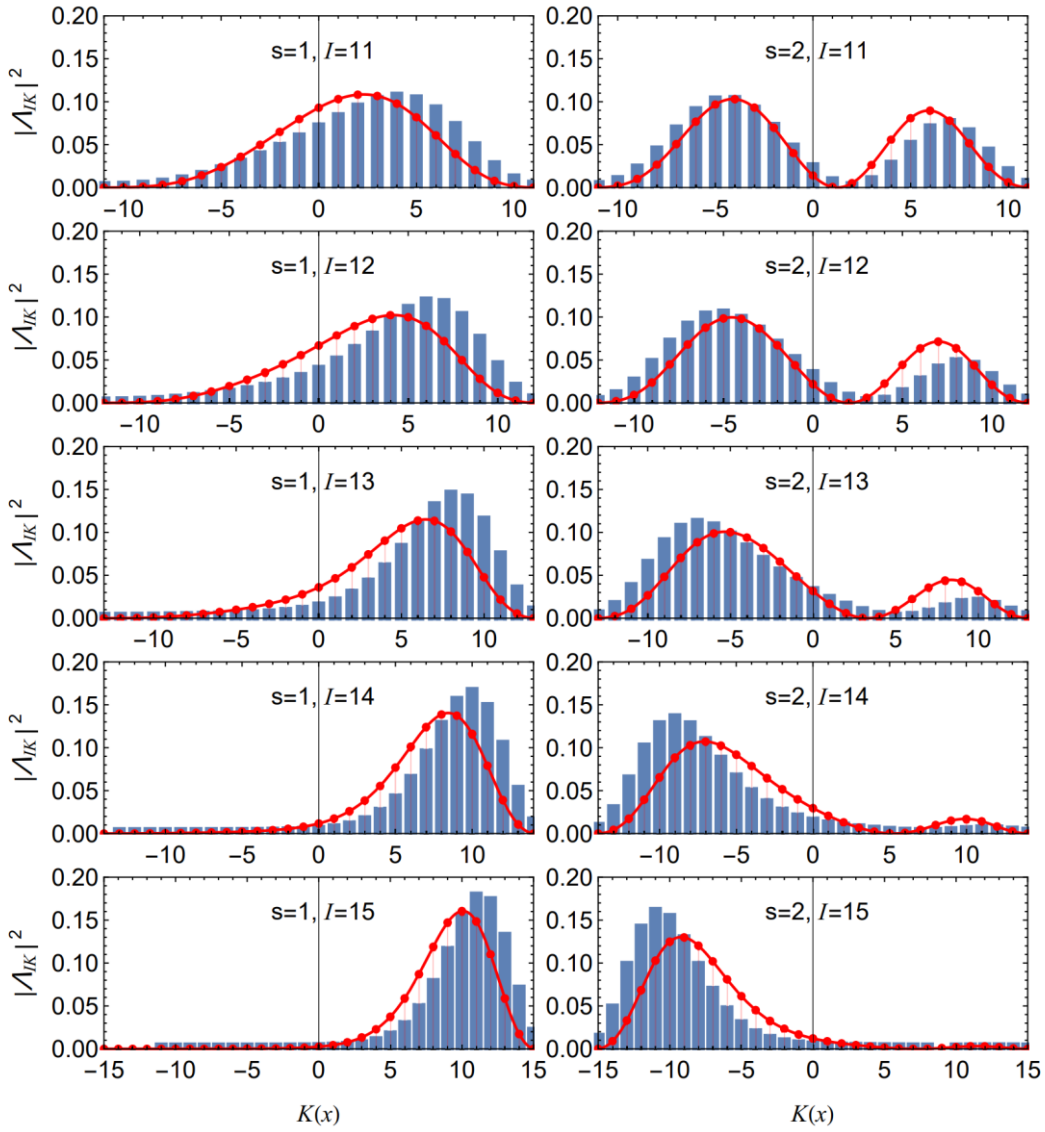

Figure 6: The total wave function components Λ_{IK} of the first (s = 1) and second (s = 2) solutions spread over K = -I, -I + 1, ..., I - 1, I, determined from the exact diagonalization of equation (2.6) (blue histogram) and deduced from the Schrödinger equation (3.10) (red circles) when $\gamma = 90°$ and $\alpha = 0°$, $\alpha' = 8°$, matching the experimental data fits for the ^{138}Pm nucleus. The continuous line represents the density distribution $\rho_I^s(x) = |F_I^s(x)|^2$ in respect to the dx metric.

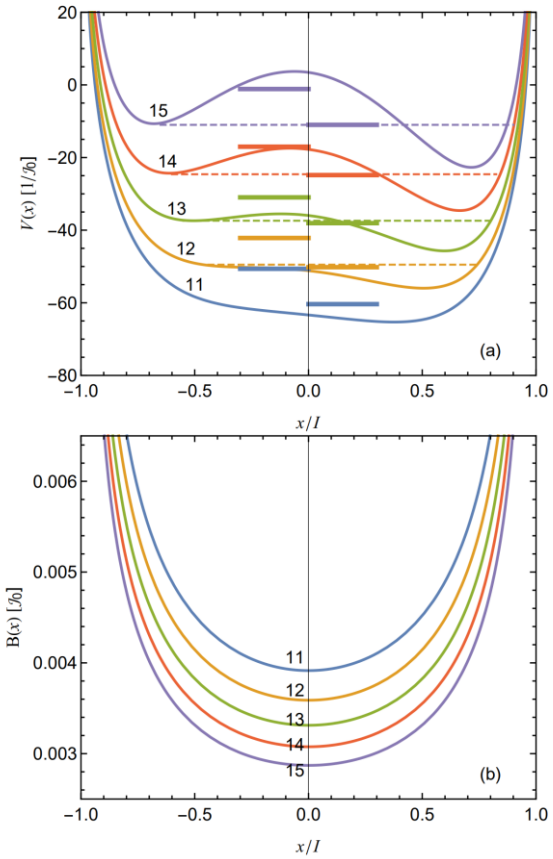

Figure 7: The evolution with total angular momentum of the quantum chiral potential $V(x)$ (a) and of the B(x) mass function (b), obtained from the numerical application on ^{138}Pm nucleus for the states I = 11, 12, 13, 14 and 15. The first two excited states, s = 1 (right) and s = 2 (left), are visualized for each angular momentum relative to their corresponding potentials.

5. Conclusions

The chiral geometry in atomic nuclei was modeled by means of a rigid alignment hypothesis applied to a Particle-Rotor Model extended to two quasiparticles. The rigid or frozen alignment approximation renders the relevant part of the Particle-Rotor Hamiltonian to a form of a simple rotor for the total angular momentum constrained by cranking terms resulting from the quasiparticle alignments. The resulted quantum problem is solved in the space of angular momentum states. Alternatively, one constructed a Schrödinger equation for a continuous projection variable, by means of a semiclassical description of the same cranked Rotor Hamiltonian. The two approaches are compared to each other in regard to the

corresponding energy spectra, in order to ascertain the deformation and alignment conditions for their equivalence. It is found, that although the results are quantitatively different, the spectral properties and different dynamical regimes of the chiral partner bands are qualitatively similar in both cases. A possible correspondence of the energy difference between the partner bands calculated in the two approaches is identified and proposed for the optimization of numerical applications. The two formalisms were also confronted in what concerns the properties of their corresponding wave function. This is realized by taking as a concrete example, the chiral partner bands observed in the ^{138}Pm nucleus. It thus found that both models provide the same evolution of the wave function with the total angular momentum, which is transiting from a vibrational regime towards a stable rotation mode where the partner bands have well established opposite handedness. In conclusion, the Schrödinger equation is a good approximation for the exact diagonalization results for low and intermediate spin values when the core's shape is very triaxial. Otherwise, the Schrödinger equation approach can be considered as a stand alone model with similar spectral features and dynamic behavior to those of the exact problem.

REFERENCES

[1] S. Frauendorf and J. Meng, Nucl. Phys. A **617**, 131 (1997).
[2] K. Starosta *et al.*, Phys. Rev. Lett. **86**, 971 (2001).
[3] B. W. Xiong and Y. Y. Wang, At. Data Nucl. Data Tables **125**, 193 (2019).
[4] Shou-Yu Wang, Chinese Phys. C **44**, 112001 (2020).
[5] S. Guo *et al.*, Phys. Lett. B **807**, 135572 (2020).
[6] Y. Zhang, B. Qi, and S. Q. Zhang, Sci. China Phys. Mech. Astron. **64**, 122011 (2021).
[7] J. Meng, J. Peng, S. Q. Zhang, and S. G. Zhou, Phys. Rev. C **73**, 37303 (2006).
[8] B. F. Lv *et al.*, Phys. Rev. C **98**, 044304 (2018).
[9] R. Budaca, Phys. Rev. C **98**, 014303 (2018).
[10] R. Budaca, Phys. Lett. B **797**, 134853 (2019).
[11] R. Budaca, Bulg. J. Phys. **46**, 411 (2019).
[12] R. Budaca, J. Phys.: Conf. Ser. **1555**, 012013 (2020).
[13] R. Budaca, Bulg. J. Phys. **48**, 467 (2021).
[14] E. A. Lawrie and O. Shirinda, Phys. Lett. B **689**, 66 (2010).
[15] A. Bohr and B. R. Mottelson, *Nuclear Structure*, Vol. 2 (Benjamin, Reading, Massachusetts, 1975).
[16] S. Frauendorf, Nucl. Phys. A **557**, 259c (1993).
[17] J. Peng, J. Meng, and S. Q. Zhang, Phys. Rev. C **68**, 044324 (2003).
[18] T. Koike, K. Starosta, and I. Hamamoto, Phys. Rev. Lett. **93**, 172502 (2004).
[19] K. Higashiyama and N. Yoshinaga, Eur. Phys. J. A **33**, 355 (2007).
[20] S. G. Rohozinski, L. Prochniak, K. Starosta, and C. Droste, Eur. Phys. J. A **47**, 90 (2011).
[21] K. Starosta and T. Koike, Phys. Scr. **92**, 093002 (2017).

[22] Q. B. Chen, N. Kaiser, Ulf-G. Meifiner, and J. Meng, Phys. Rev. C **99**, 064326 (2019).
[23] V. I. Dimitrov, S. Frauendorf, and F. Donau, Phys. Rev. Lett. **84**, 5732 (2000).
[24] A. A. Hecht *et al.*, Phys. Rev. C **63**, 051302(R) (2001).
[25] P. Olbratowski, J. Dobaczewski, J. Dudek, and W. Plociennik, Phys. Rev. Lett. **93**, 052501 (2004).
[26] P. W. Zhao, Phys. Lett. B **773**, 1 (2017).
[27] S. Mukhopadhyay *et al.*, Phys. Rev. Lett. **99**, 172501 (2007).
[28] D. Almehed, F. Donau, and S. Frauendorf, Phys. Rev. C **83** (2011) 054308.
[29] Q. B. Chen, S. Q. Zhang, P. W. Zhao, R. V. Jolos, and J. Meng, Phys. Rev. C **87**, 024314 (2013).
[30] Q. B. Chen, S. Q. Zhang, P. W. Zhao, R. V. Jolos, and J. Meng, Phys. Rev. C **94**, 044301 (2016).
[31] X. H. Wu, Q. B. Chen, P. W. Zhao, S. Q. Zhang, and J. Meng, Phys. Rev. C **98**, 064302 (2018).
[32] A. A. Raduta, C. M. Raduta, and A. Faessler, J. Phys. G: Nucl. Part. Phys. **41**, 035105 (2014).
[33] A. A. Raduta, Al. H. Raduta, and C. M. Petrache, J. Phys. G: Nucl. Part. Phys. **43**, 095107 (2016).
[34] G. H. Bhat, J. A. Sheikh, and R. Palit, Phys. Lett. B **707**, 250 (2012).
[35] F. Q. Chen, J. Meng, and S. Q. Zhang, Phys. Lett. B **785**, 211 (2018).
[36] M. Shimada, Y. Fujioka, S. Tagami, and Y. R. Shimizu, Phys. Rev. C **97**, 024319 (2018).
[37] R. Budaca, Phys. Lett. B **817**, 136308 (2021).
[38] R. Budaca, Front. Phys. **19**, 24301 (2024).
[39] D. Tonev *et al.*, Phys. Rev. C **76**, 044313 (2007).
[40] S. Brant, D. Tonev, G. de Angelis, and A. Ventura, Phys. Rev. C **78**, 034301 (2008).
[41] H. G. Ganev, A. I. Georgieva, S. Brant, and A. Ventura, Phys. Rev. C **79**, 044322 (2009).
[42] R. Budaca, Phys. Rev. C **97**, 024302 (2018).
[43] R. Budaca, Phys. Rev. C **103**, 044312 (2021).
[44] B. F. Lv *et al.*, Phys. Rev. C **105**, 034302 (2022).
[45] R. Budaca and C. M. Petrache, Phys. Rev. C **106**, 014313 (2022).
[46] R. Budaca and A. I. Budaca, J. Phys. G: Nucl. Part. Phys. **50**, 125101 (2023).
[47] S. Frauendorf and F. Donau, Phys. Rev. C **89**, 014322 (2014).
[48] A. A. Raduta, R. Budaca, and C. M. Raduta, Phys. Rev. C **76**, 064309 (2007).
[49] R. Budaca, Ann. Acad. Rom. Sci. Ser. Math. Appl. **11**, 115 (2019).
[50] K. Y. Ma *et al.*, Phys. Rev. C **97**, 014305 (2018).
[51] P. Siwach, P. Arumugam, L. S. Ferreira, and E. Maglione, Phys. Lett. B **811**, 135937 (2020).